

## Article

# Calcium Sulfate Nanoparticles in Surface Sediments of Lingding Bay of the Pearl River Estuary, China: Implications for the Nonclassical Crystallization Pathway of Gypsum in the Natural Estuary Environment

Guoqiang Wang <sup>1</sup>, Tianjian Yang <sup>2,\*</sup>, Yitong Fan <sup>1</sup>, Shushu Bai <sup>1</sup> and Peiyuan Yin <sup>1</sup>

<sup>1</sup> School of Geographical Sciences, Shanxi Normal University, Taiyuan 030031, China; wangguoqiang@sxnu.edu.cn (G.W.)

<sup>2</sup> South China Institute of Environmental Sciences, Ministry of Ecology and Environment, Guangzhou 510655, China

\* Correspondence: yangtianjian@scies.org

**Abstract:** The mechanism of the nonclassical crystallization pathway of calcium sulfate dihydrate (gypsum) with calcium sulfate hemihydrate (bassanite) as a precursor has been considered in many studies. However, studies on the crystallization of gypsum in natural environments have rarely been reported, especially with regard to natural estuaries, which are one of the most important precipitation environments for calcium sulfate. Here, surface sediments (0–5 cm) of Lingding Bay of the Pearl River Estuary in China were sampled and analyzed. X-ray powder diffraction (XRD) analysis showed that calcium sulfate in the surface sediments mainly existed in the form of gypsum. In high-resolution transmission electron microscopy (HR-TEM) analysis, calcium sulfate nanoparticles were observed in the surface sediments. These particles mainly included spherical calcium sulfate nanoparticles (diameter ranging from 10–50 nm) and bassanite nanorod clusters (sizes ranging from 30 nm × 150 nm to 100 nm × 650 nm), and their main elements included O, S and Ca, with small amounts of N, Si, Na and Mg. The bassanite nanorods self-assembled into aggregates primarily co-oriented along the c axis (i.e., [001] direction). In epitaxial growth into larger bassanite nanorods (100 nm × 650 nm), the crystal form of gypsum could be observed. Based on the observations and analyses, we proposed that the crystallization of gypsum in surface sediments of the natural estuary environment could occur through the nonclassical crystallization pathway. In this pathway, bassanite nanoparticles and nanorods appear as precursors (nanoscale precursors), grow via self-assembly, and are finally transformed into gypsum. This work provided evidence supporting and enhancing the understanding of the crystallization pathway of calcium sulfate phases in the natural estuary environment. Furthermore, the interactions between calcium sulfate nanoparticles and the natural estuary environment were examined.



**Citation:** Wang, G.; Yang, T.; Fan, Y.; Bai, S.; Yin, P. Calcium Sulfate Nanoparticles in Surface Sediments of Lingding Bay of the Pearl River Estuary, China: Implications for the Nonclassical Crystallization Pathway of Gypsum in the Natural Estuary Environment. *Minerals* **2023**, *13*, 903. <https://doi.org/10.3390/min13070903>

Academic Editor: Hermann Kudrass

Received: 6 June 2023

Revised: 22 June 2023

Accepted: 30 June 2023

Published: 3 July 2023

**Keywords:** transmission electron microscopy (TEM); calcium sulfate nanoparticles; surface sediment; crystallization



**Copyright:** © 2023 by the authors. Licensee MDPI, Basel, Switzerland. This article is an open access article distributed under the terms and conditions of the Creative Commons Attribution (CC BY) license (<https://creativecommons.org/licenses/by/4.0/>).

## 1. Introduction

Calcium sulfate is widely found in the Earth's crust, in areas such as deserts, lakes and oceans [1,2]. Calcium sulfate has three crystalline polymorphs that differ in their degree of hydration, including dihydrate ( $\text{CaSO}_4 \cdot \text{H}_2\text{O}$ , gypsum), hemihydrate ( $\text{CaSO}_4 \cdot 0.5\text{H}_2\text{O}$ , bassanite) and anhydrite ( $\text{CaSO}_4$ ) [3–6]. Among these polymorphs, gypsum is the most stable phase at room temperature and has a wide range of uses in different fields, such as soil amendments, cement additives, and roadbed substrates [2,3,6]. Moreover, solid calcium sulfate can be used for water purification in seawater desalination plants, oil recovery and mining activities [7–9]. However, in the above production process, calcium sulfate always

precipitates and covers the surface of pipelines and heat exchangers, thereby posing a serious economic threat [10,11]. Therefore, delaying or preventing calcium sulfate scaling introduces an industrial technical problem that urgently must be solved. More in-depth studies on the crystallization mechanism of calcium sulfate are needed. Furthermore, gypsum is an extremely important index mineral in geological evolution and is used to reflect the behavior of water molecules in planetary history [12–14]. As an important sulfur-containing mineral, calcium sulfate also plays an important role in the global sulfur cycle [11]. Therefore, the research on the crystallization process of calcium sulfate can contribute to many fields.

According to classical crystal growth theory, calcium sulfate crystals are grown via the continuous aggregation or unit replication of calcium ions ( $\text{Ca}^{2+}$ ) and sulfate ions ( $\text{SO}_4^{2-}$ ) on the surface of calcium sulfate nuclei [15–17]. In recent years, electron microscopy techniques have seen great progress, especially high-resolution transmission electron microscopy (HR-TEM), which has been widely used in the field of mineralogy. In these studies, researchers have made many new discoveries regarding the crystallization and growth mechanism of calcium sulfate (mainly gypsum), which differ from the classical theory [3,11]. It has been suggested that gypsum may be precipitated first by nanoscale precursors (e.g., amorphous or calcium sulfate hemihydrate nanoparticles) at the early stage of nucleation and growth, and then transformed into a stable phase as gypsum via directional aggregation [2–6,11,18–20].

Previous studies were mostly based on experiments involving artificially prepared saturated solutions. However, studies on the crystallization of calcium sulfate in natural environments have rarely been reported, especially with regard to marine environments. The marine environment is one of the most important precipitation environments for calcium sulfate today [2]. As a sea–land intersection, the estuary area in marine environments is a key area for material migration and circulation [21]. Moreover, many large gypsum deposits were formed in the marine environment during geological history [6,11]. Therefore, it is typical and necessary to study the crystallization of calcium sulfate in the estuary area of rivers.

Nanoparticles have specific properties due to an increased surface-to-volume ratio and particle quantum effects [22,23]. Due to their extremely small size and high mobility, nanoparticles do not rapidly precipitate after formation in seawater [24]. Thus, they could migrate over long distances with sea water flow. Furthermore, nanoparticles have the potential to enter the biological body and affect the health of organisms [25–27]. Therefore, through the investigation of calcium sulfate nanoparticles in surface sediments of Lingding Bay, we explored the interactions between calcium sulfate nanoparticles and the natural environment.

Lingding Bay of the Pearl River Estuary was selected as the research area, and the Pearl River is the third largest river in China. In the middle and upper reaches of the Pearl River, it flows through the very large karst landform area and finally transports and deposits a large amount of calcareous minerals in the Pearl River Estuary (mainly into Lingding Bay, Figure 1a,b). Therefore, this region is an excellent place to study the crystallization and precipitation of calcareous minerals (including calcium sulfate). In this study, we use high-resolution transmission electron microscopy (HR-TEM) as our primary probing technique to investigate the characteristics of calcium sulfate nanoparticles in surface sediments. This study could provide a new understanding of the crystallization pathway of calcium sulfate in natural environments. Furthermore, the interactions between calcium sulfate nanoparticles and the natural environment are examined.

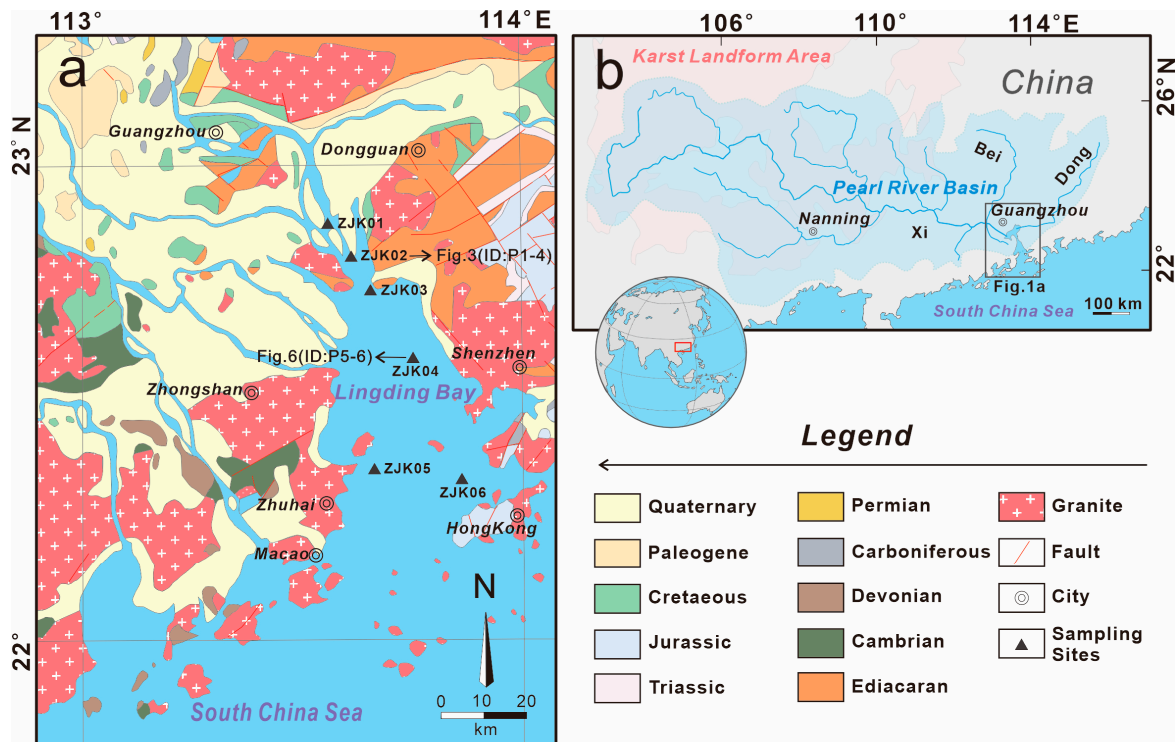


**Figure 1.** (a) Sketch map of the Pearl River Estuary and locations of the sampling sites in the Lingding Bay (modified from the geological map published by the China Geological Survey). (b) Water system map of the Pearl River Basin (modified by the authors of [28]).

## 2. Geological Setting

The Pearl River Basin covers an area of 425,700 km<sup>2</sup>, with a total length of 2320 km, making it the third-longest river in China (Figure 1b; [28,29]). The Pearl River system consists of major tributaries, namely the Xi, Bei and Dong Rivers (in Chinese, xi = west, bei = north, and dong = east), which converge near Guangzhou and eventually flow into the Pearl River Estuary. The Pearl River Basin is located from 22° N to 26° N. The region has a subtropical monsoon climate, with an average annual temperature ranging from 14 °C to 22 °C and average annual rainfall of 1.5m [30,31]. The average annual runoff and the average annual sediment load in the Pearl River Basin are 342.1 km<sup>3</sup>/yr and 74.30 Mt/yr, respectively (Pearl River Sediment Bulletin, 2021).

The Pearl River Estuary is located at 21°50′–23°25′ N and 112°33′–114°10′ E, in the southernmost part of the Pearl River Basin. The Pearl River Delta, where the research area is located, is one of the most economically developed regions in China, with several economically developed cities such as Guangzhou, Shenzhen, Hong Kong and Macao (Figure 1a). The area has a developed water system and convenient shipping conditions. The entire Pearl River Estuary is located in the northern part of the South China Sea, and its main sea area is Lingding Bay, which is also the study area. It covers an area of approximately 2000 km<sup>2</sup>, and the average depth of sea water is less than 30 m (Figure 1a,b; [28,32]).

The sediments of Lingding Bay in the Pearl River Estuary mainly encompass various geological units in the basin. The main rock types include upper Paleozoic carbonate rocks, Emeishan basalt and Permian dolomite in the Xi River Basin; Yanshan period granites and Paleozoic carbonates in the Bei River Basin; and Jurassic sandstones and mudstones in the Dong River Basin [33,34]. The various rock types in the basin provide abundant terrigenous materials for the lower Pearl River Estuary. In particular, the tributaries of the Xi River flow through the largest karst landform area in southern China (Figure 1b; [35,36]), transporting a large amount of calcium components entering Lingding Bay, providing a material foundation for the formation and deposition of calcium minerals.

### 3. Materials and Methods

#### 3.1. Sampling Location and Methods

In total, 6 surface sediment samples (0–5 cm) were collected at 6 sample sites with a water depth of 20 m in the lower reaches of the Pearl River Estuary (ZJK01-06, Figure 1a). These sediment samples were obtained using a stainless-steel grab sampler. The samples were mainly a muddy, yellow to brownish-yellow. Samples ZJK01, ZJK02, ZJK05 and ZJK06 were muddy-silty and had brown to yellow color. Sample ZJK03 was muddy and gray to green in color. Sample ZJK04 was muddy-silty and had a brownish color. After sampling, the sediments were placed in sterile polyethylene bags and stored at 4 °C until further laboratory analysis.

#### 3.2. Analytical Methods

A part of each sample was taken out for the X-ray powder diffraction (XRD) analysis. Before XRD analysis, the samples were first pretreated. They were dried in a thermostatic chamber at 50 °C for 24 h. After cooling, the samples were placed in separate sample bags. Afterward, they were passed through a 200-mesh sieve, and analyzed via XRD using a Rigaku SmartLab X-ray diffractometer (Tokyo, Japan) with Cu radiation in the 2 $\theta$  range from 10° to 90° and a scan rate of 4°/min. The operating conditions included a 40 kV voltage and 100 mA current. The XRD spectra were processed in MDI Jade 6.5 equipped with the PDF 2-2004 database.

Another part of each sample was taken out for high-resolution transmission electron microscopy (HR-TEM) analysis. Structural/chemical information on the samples was obtained using a transmission electron microscopy (TEM) instrument (FEI Talos F200X) equipped with an energy-dispersive X-ray spectra (EDS) detector. The general steps for sample preparation were as follows. (I) A minute quantity of the muddy sample was taken with a tweezer and smeared on the TEM grid. (II) Subsequently, the TEM grid was clipped by another clean tweezer and placed on the surface of sterile filter paper that absorbed the pore water of the sediment. (III) After that, the TEM grid was clipped with the tweezer, and the obvious impurity particles were blown off with a rubber pipette bulb. (IV) Steps (II) and (III) were repeated until there was no obvious moisture and until there were no impurities on the TEM grid. TEM observation was performed immediately after sample preparation. The specific parameters of the test instruments were as follows. The maximum accelerating voltage was 200 kV, the dot resolution was 0.20 nm, the linear resolution was 0.14 nm, the high-angle annular dark-field scanning transmission electron microscope (HAADF-STEM) imaging resolution was 0.16 nm, and the maximum magnification of the TEM and STEM devices were 1.5 million and 2.3 million times, respectively. The morphological features, EDS, HR-TEM image, and selected area electron diffraction (SAED) patterns of the nanoparticles were obtained. Cu/Mo-C TEM grids were used in this test, and the C and Cu/Mo contents were not considered in the EDS results.

All of the analyses in this study were conducted at the Sinoma Institute of Materials Research (Guangzhou) Co., Ltd., Guangzhou, China.

### 4. Results

#### 4.1. Mineral Composition of the Surface Sediments

According to the XRD analysis results (Figure 2), the main mineral components of the surface sediments of Lingding Bay were similar, mainly including quartz, muscovite, plagioclase, potassium feldspar, clay minerals (montmorillonite, illite and chlorite), calcite and gypsum. The minerals in the surface sediments of Lingding Bay were mainly derived from the physical and chemical weathering of rocks in the Pearl River Basin and then transported to the estuary, after which they were precipitated. Among them, calcium sulfate mainly existed as gypsum (CaSO<sub>4</sub>·H<sub>2</sub>O). The XRD patterns of the surface sediment samples showed sharp peaks at 11.7° and 29.1°, which corresponded to the (020) and (041) planes of gypsum (Figure 2, ZJK02-06), respectively. A small amount of gypsum may have been produced during the drying process of the sample. Considering that calcium sulfate

is slightly soluble in water, the calcium sulfate crystals produced in the pore water were very limited, and most of the gypsum was naturally formed.

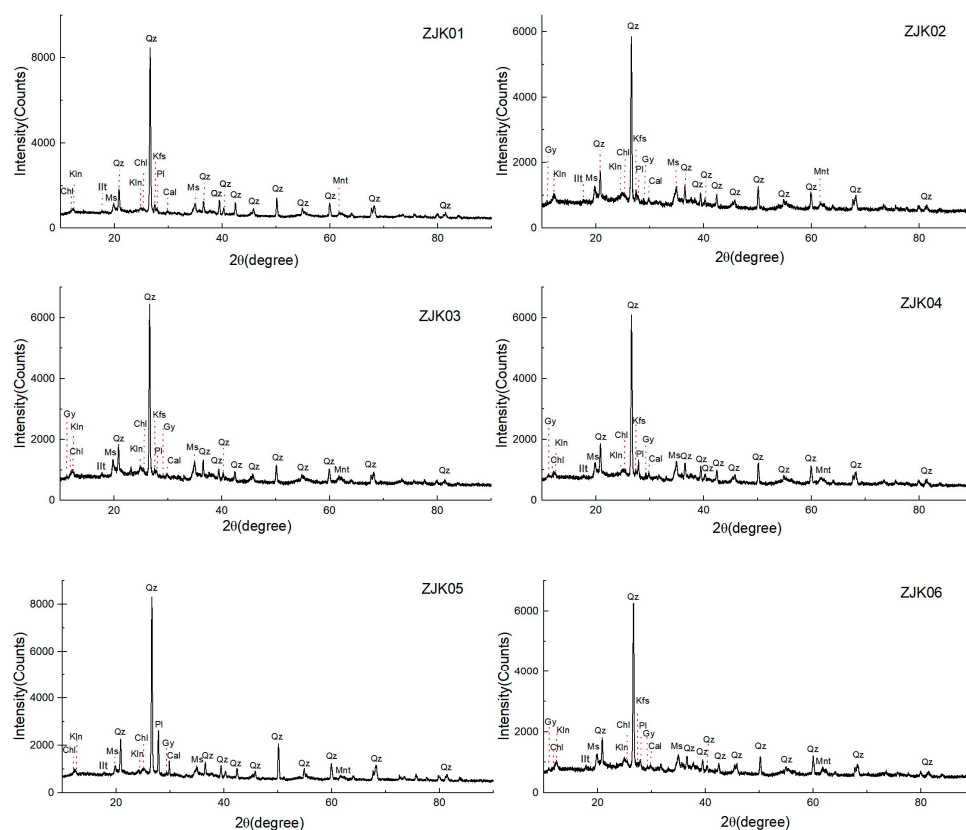


**Figure 2.** The XRD analysis results for the surface sediments. Chl, chlorite; Gy, gypsum; Ill, illite; Kfs, K-feldspar; Kln, kaolinite; Ms, muscovite; Mnt, montmorillonite; Pl, plagioclase; Qz, quartz.

#### 4.2. Characteristics of Calcium Sulfate Nanoparticles in the Surface Sediments

Numerous calcium sulfate nanoparticles were found in the surface sediment samples. The microscopic characteristics of representative nanoparticles were selected and analyzed in detail (Figures 3–7, Table 1). Morphological analysis showed that the nanoparticles in the surface sediments mainly appeared as nanorods (Figures 3a and 6a) or spherical particles (Figure 6f), and most of the calcium sulfate nanoparticles were aggregates.

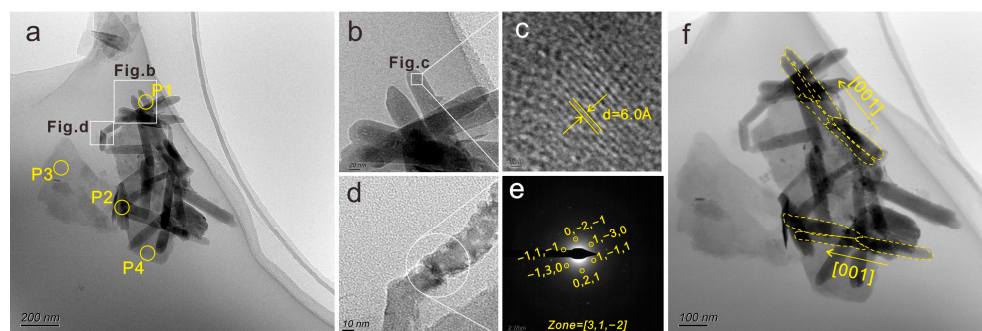


**Figure 3.** (a) TEM image of bassanite nanorod clusters and layered silicate nanoparticles (ID: P1–P4, Figure 4 and Table 1); (b,c) HR-TEM images of bassanite nanorods with characteristic 6.0 Å d-spacing for bassanite; (d,e) HR-TEM image and SAED pattern of bassanite nanorods in another position, and showing the SAED pattern corresponding to the zone axis =  $[3\bar{1}2]$  of bassanite; (f) TEM image of bassanite nanorods prior to oriented aggregation along the c axis (i.e.,  $[001]$  direction), marked with yellow lines for ease of viewing.

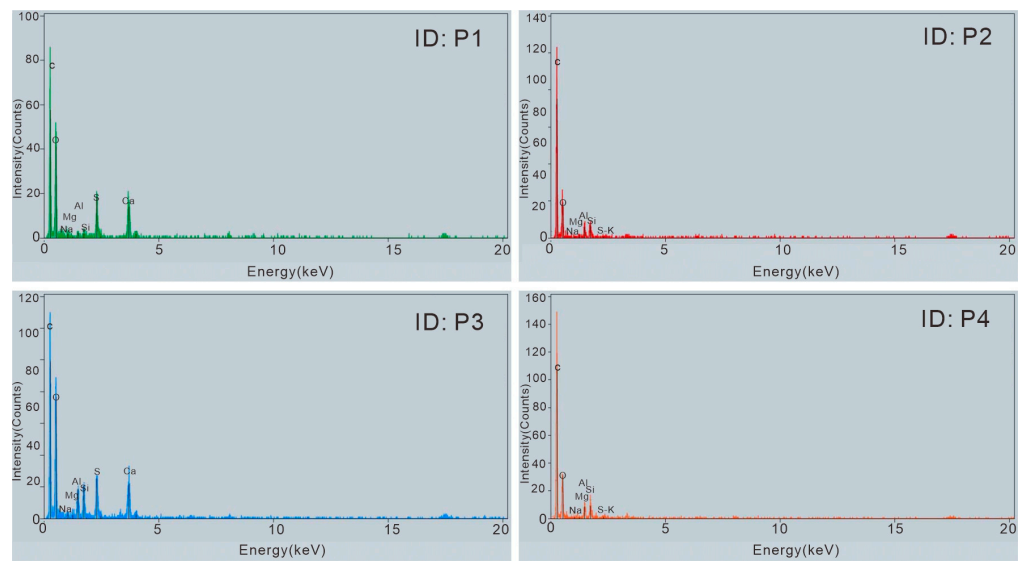


Figure 4. EDS images of bassanite nanorod clusters and layered silicate nanoparticles (ID: P1–P4).

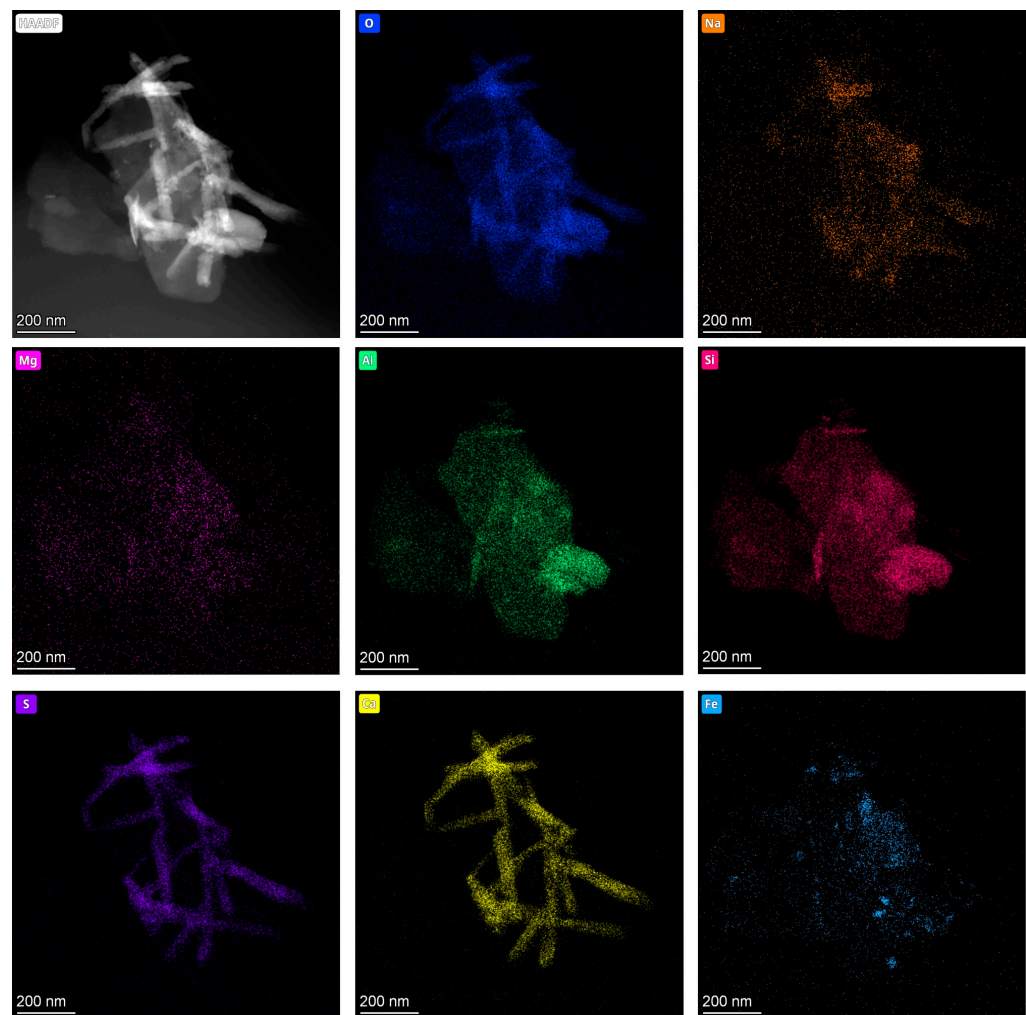
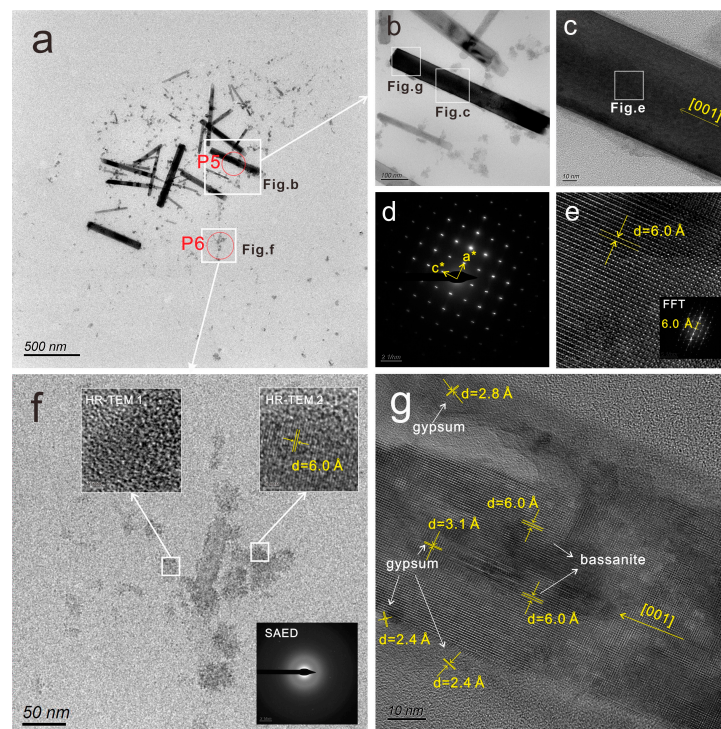
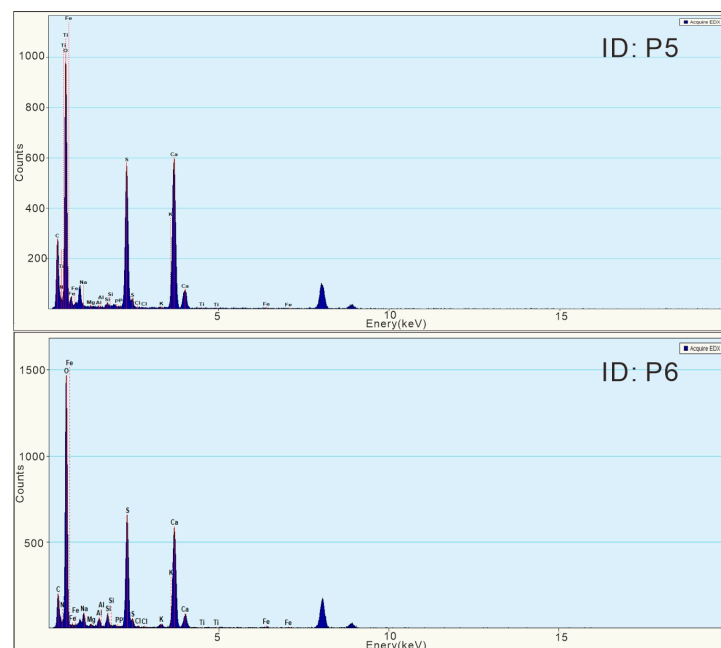


Figure 5. HAADF-STEM image and O, Na, Mg, Al, Si, S, Ca and Fe TEM maps of the bassanite nanorod clusters attached to layered silicate nanoparticles.



**Figure 6.** (a) TEM image of bassanite nanorod clusters and spherical calcium sulfate nanoparticles—the EDS results (ID: P5–P6) are shown in Figure 7 and Table 1; (b,c) HR-TEM images of a bassanite nanorod; (d) SAED pattern of (c), showing the pattern corresponding to the reciprocal lattice of bassanite along the a and c axes; (e) HR-TEM images and fast Fourier transform (FFT) pattern of (c), with characteristic 6.0 Å d-spacing for bassanite; (f) TEM image of the aggregation of spherical calcium sulfate nanoparticles—the SAED pattern and HR-TEM 1 indicate mainly amorphous aggregation, and HR-TEM 2 shows characteristic 6.0 Å d-spacing for bassanite; (g) HR-TEM images of (c), showing the detailed information of the epitaxial growth of bassanite nanorods, with marked lattice spacings corresponding to bassanite (6.0 Å) and gypsum (3.1 Å, 2.8 Å and 2.4 Å).



**Figure 7.** EDS images of bassanite nanorod clusters and spherical calcium sulfate nanoparticles (ID: P5–P6).

**Table 1.** EDS results for the nanoparticles in the sediment samples of Lingding Bay (ID: P1–P6).

Sample No.	EDS ID	Particle Type	Element	N	O	Na	Mg	Al	Si	P	S	Cl	K	Ca	Ti	Fe
ZJK02	P1	Calcium sulfate nanorod	Weight %		46.48	1.98	0.62	2.90	2.47		20.83			24.73		
			Atomic %		64.88	1.93	0.56	2.41	1.96		14.49				13.78	
ZJK02	P2	Calcium sulfate nanorod attached to silicate nanoparticle	Weight %		41.84	1.86	1.14	9.07	10.63		17.07			18.39		
			Atomic %		58.77	1.83	1.07	7.55	8.50		11.97				10.31	
ZJK02	P3	Layered silicate nanoparticle	Weight %		53.60	1.69	3.62	17.48	20.99		2.62					
			Atomic %		66.32	1.48	2.96	12.82	14.76		1.65					
ZJK02	P4	Layered silicate nanoparticle	Weight %		54.38	1.93	1.65	18.94	20.43		2.67					
			Atomic %		67.17	1.63	1.34	13.85	14.38		1.63					
ZJK04	P5	Calcium sulfate nanorods	Weight %	2.55	48.89	0.43	0.04		0.28	0.20	21.38	0.12	0.11	25.93		0.06
			Atomic %	3.97	66.51	0.40	0.03		0.21	0.14	14.51	0.07	0.06	14.08		0.01
ZJK04	P6	Spherical calcium sulfate nanoparticles	Weight %	2.41	50.95	2.07	0.22	1.43	2.11	0.08	18.29	0.17	0.39	21.71	0.17	
			Atomic %	3.64	67.53	1.91	0.19	1.12	1.60	0.05	12.09	0.10	0.21	11.49	0.07	

The calcium sulfate nanorods tended to aggregate into clusters, as shown in Figure 3a. More than 20 nanorods gathered together and were attached to layered nanoparticles, and the single nanorod size was approximately 60 nm × 250 nm. The primary compositions of the nanorods at the P1 position included O, S and Ca, with small amounts of Na, Mg, Al and Si (Table 1 and Figure 4; ID: P1). Combined with the element distribution TEM maps shown in Figure 5, the components of the nanorods primarily included Ca, S and O, indicating that they were calcium sulfate nanorods. In the HR-TEM images (Figure 3b–e), the characteristic 6.0 Å d-spacing of calcium sulfate hemihydrate ( $\text{CaSO}_4 \cdot 0.5\text{H}_2\text{O}$ ; bassanite) was observed. In addition, the SAED pattern of another nanorod showed a SAED pattern corresponding to the zone axis =  $[31\bar{2}]$  of bassanite. Therefore, the analysis results suggested that these nanorods mainly occurred in the form of bassanite. Simultaneously, the TEM image (Figure 3f) showed that the bassanite nanorods self-assembled into aggregates primarily co-oriented along the c axis (i.e.,  $[001]$  directions) to form into larger nanorods.

The EDS results for other positions (Table 1 and Figure 4, ID: P3–P4) in Figure 3a primarily included O, Si and Al, with small amounts of Na, Mg and S, suggesting that the layered particles were silicates. In addition, the EDS result indicated that the P2 position of Figure 3a contained both calcium sulfate and silicate (Table 1 and Figure 4, ID: P2). The HAADF-STEM image and element TEM distribution (Figure 5) showed that the bassanite nanorods and Fe-bearing nanoparticles were adsorbed onto the surface of layered silicate nanoparticles.

Figure 6a shows about approximately 25 calcium sulfate nanorods, with nanorod sizes ranging from 30 nm × 150 nm to 100 nm × 650 nm. Most of them are larger than the nanorods observed in Figure 3a. The EDS results (Table 1 and Figure 7, ID: P5) showed that the main components of the nanorods included O, S and Ca, with a minor amount of N, Na, Mg, Si, etc. More morphological and lattice details of the calcium sulfate nanoparticles are shown in Figure 6b,c. Figure 6d shows the SAED pattern corresponding to the reciprocal lattice of bassanite along the a and c axes. Meanwhile, a characteristic 6.0 Å d-spacing for bassanite was observed, as shown in Figure 6e. Based on the above information, these nanorods also appeared in the form of bassanite. However, Figure 6g shows the detailed information on the epitaxial growth of bassanite nanorods, with marked lattice spacings corresponding to bassanite (6.0 Å) and gypsum (3.1 Å, 2.8 Å and 2.4 Å), indicating that the crystal form of gypsum existed during the epitaxial growth of the nanorods.

Moreover, numerous spherical nanoparticle aggregates were observed, as shown in Figure 6a. Typical nanoparticle aggregates were observed and analyzed in detail (Figure 6e). These spherical nanoparticles exhibited a diameter of 10–50 nm, and their main elements included O, S and Ca, with small amounts of N, Si, Na and Mg (Table 1 and Figure 7, ID: P6), which is similar to the compositions of the surrounding nanorods. According to the SAED pattern and HR-TEM image (Figure 6e, SAED and HR-TEM 1, respectively), these nanoparticles were mainly amorphous. In the HR-TEM image for another position (Figure 6e, HR-TEM 2), the characteristic 6.0 Å d-spacing of bassanite (6 Å) was observed, indicating that a few of their crystalline forms included bassanite.

## 5. Discussion

### 5.1. Implication for the Nonclassical Crystallization Pathway of Calcium Sulfate Dihydrate (Gypsum) in the Natural Estuary Environment

According to classical crystal growth theory, calcium sulfate crystals are grown via continuous aggregation or the unit replication of calcium ions ( $\text{Ca}^{2+}$ ) and sulfate ions ( $\text{SO}_4^{2-}$ ) on the surface of calcium sulfate nuclei [15–17]. In recent years, researchers have deeply studied the nucleation and crystallization process of calcium sulfate dihydrate (gypsum) in a saturated solution of calcium sulfate at room temperature [2–6,11,18–20,37]. Based on previous studies, the mechanism of the nonclassical crystallization pathway of gypsum with calcium sulfate hemihydrate (bassanite) as a precursor was proposed and constantly improved [2–4,11,37]. A schematic diagram is shown in Figure 8. The main process includes the following stages. (I) Initially, amorphous calcium sulfate nanoparticles

precipitate from the solution saturated with  $\text{Ca}^{2+}/\text{SO}_4^{2-}$  [3,37], and they then crystallize into bassanite nanoparticles as the nanoscale precursor emerges [3,11,19,37]. (II) Bassanite nanoparticles grow into nanorods, and bassanite nanorods self-assemble into aggregates primarily co-oriented along the *c* axis (i.e., [001] direction), to form larger-size nanorods. (III) The large-size nanorods are finally transformed into gypsum [2,11,18]. Certainly, nonclassical pathways commonly exist in the crystallization process of minerals, and the types of precursors vary [38–41].

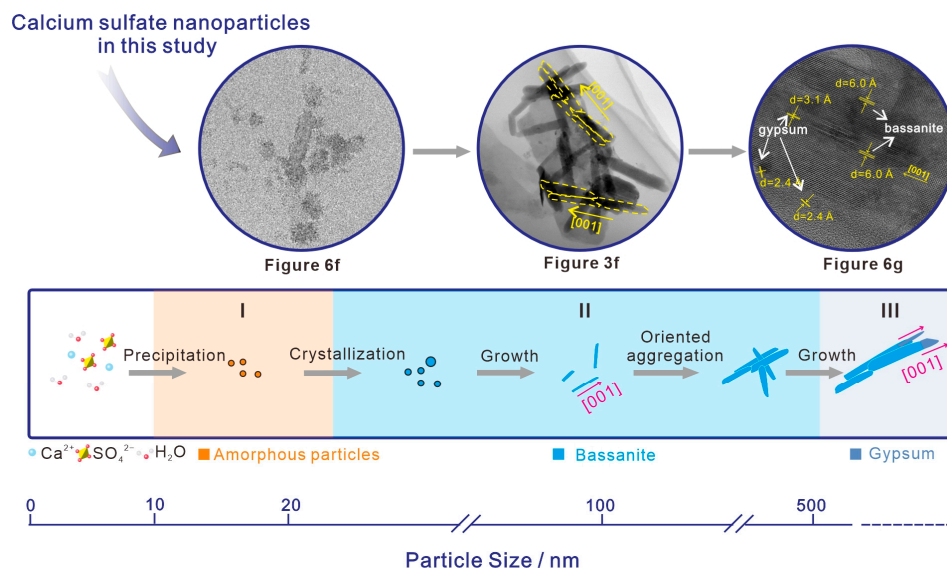


**Figure 8.** Schematic of nonclassical particle assembly growth of bassanite, followed by heterogeneous nucleation and epitaxial growth of gypsum (according to [2,3]).

In this study, in the surface sediments of Lingding Bay, calcium sulfate mainly occurred in the form of gypsum (Figure 2), which is the most stable phase at room temperature [3]. However, based on the TEM analysis, many calcium sulfate nanoparticles and nanorods (Figures 3a and 6a) appeared in the form of metastable-phase bassanite (Figure 6f). We propose that bassanite nanoparticles and nanorods appeared as precursors, grew in the nonclassical crystallization pathway, and finally transformed into gypsum. Various pieces of evidence were observed corresponding to the nonclassical crystallization pathway proposed above (Figure 8). The details are as follows: (I) spherical amorphous nanoparticles (Figure 6a,f), a few of which were converted into bassanite, with a small size ranging from 5–20 nm, indicating that these particles likely appeared at the initial stage of the growth process; (II) bassanite nanorods aggregated into clusters (Figures 3a and 6a), and prior to oriented aggregation and assembly along the *c* axis (Figure 3f), the size of nanorods at this stage was approximately 60 nm × 250 nm; (III) during epitaxial growth into larger bassanite nanorods (100 nm × 650 nm), the crystal form of gypsum could be observed (Figure 6g), indicating that bassanite nanorods were further growing and transforming into gypsum.

Previous studies [2,11,18,19] have suggested that the thermodynamic stability of the three phases of calcium sulfate may overlap under small-particle-size conditions, and bassanite is more stable than gypsum under nanoscale conditions. Therefore, at the early stage of the crystallization process of calcium sulfate dihydrate (gypsum), the metastable calcium sulfate hemihydrate (bassanite) precursor often first appears as an intermediate phase. This also explains why most of the nanoscale calcium sulfates found in the surface sediments occurred in the form of bassanite.

In summary, the investigation of calcium sulfate nanoparticles in the surface sediments of Lingding Bay provided evidence supporting the existence of a nonclassical crystalliza-

tion pathway for gypsum in the natural estuary environment. Moreover, the bassanite nanoparticles first emerged as precursors in this crystallization process.

### *5.2. Implications for Interactions between Calcium Sulfate Nanoparticles and the Estuary Environment*

The nonclassical crystallization path of minerals is formed via the aggregation and directional arrangement of precursor nanoparticles [11]. The aggregation behavior of nanoparticles in natural water environments is affected by various environmental factors, such as solution pH, ionic strength, electrolyte solutions, and varied organic matter and amount [42–45]. In addition to the above factors, various other materials present in the natural water environment may affect the crystallization and precipitation process of minerals. In this study, we observed that bassanite nanorods aggregated with layered clay mineral nanoparticles (Figures 3a and 5). Layered silicate nanoparticles such as kaolinite and montmorillonite have adsorption properties [46], and the abundant presence of layered silicate nanoparticles in surface sediments may influence the crystallization, aggregation and deposition of calcium sulfate minerals.

Moreover, the sizes of the calcium sulfate nanoparticles observed in the surface sediments of Lingding Bay ranged from 50 nm × 150 nm to 100 nm × 650 nm. As nanoscale particles, they have specific properties due to an increased surface-to-volume ratio and particle quantum effects [22,23]. Owing to their extremely small size and high mobility, some nanoparticles do not precipitate rapidly after formation in seawater [24]. Thus, they can migrate over long distances with sea water flow. Furthermore, nanoparticles have potential to enter the biological body and affect the health of organisms [25–27]. In this study, we detected nitrogen (N)-bearing calcium sulfate nanoparticles in the surface sediments of Lingding Bay (Table 1, ID P5–P6). Moreover, calcium sulfate is one of the main sulfur-containing minerals in marine sediments. The migration and precipitation of N-bearing calcium sulfate nanoparticles could affect the distribution and content of N and S elements in regional seawater. Sulfur (S) and nitrogen (N) are two of the most important elements in marine ecosystems. Therefore, N-bearing calcium sulfate nanoparticles may play a certain role in elemental cycling in an estuary ecosystem.

In summary, calcium sulfate nanoparticles could interact with materials and factors in the natural estuarine bay environment, and participate in geological and ecological processes.

## **6. Conclusions**

- I. The mineral components of the surface sediments of Lingding Bay were similar, mainly including quartz, muscovite, plagioclase, potassium feldspar, clay minerals and calcareous minerals. Among them, calcium sulfate mainly existed in the form of gypsum.
- II. The calcium sulfate nanoparticles in the surface sediments of Lingding Bay were mainly spherical calcium sulfate nanoparticles (with a diameter ranging from 10 to 50 nm) and bassanite nanorod clusters (sizes ranging from 50 nm × 150 nm to 100 nm × 650 nm), and their main elements included O, S and Ca, with small amounts of N, Si, Na and Mg. The spherical calcium sulfate nanoparticles were mainly amorphous (diameter ranging from 10–50 nm), and a few of them appeared to be crystallized into bassanite. The bassanite nanorods self-assembled into aggregates primarily co-oriented along the c axis [001]. During epitaxial growth into larger bassanite nanorods (100 nm × 650 nm), the crystal form of gypsum could be observed.
- III. Based on the observations and analyses above, we propose that the crystallization of gypsum in surface sediments of the natural estuary environment could occur through the nonclassical crystallization pathway. In this pathway, amorphous calcium sulfate nanoparticles precipitate from the solution saturated with  $\text{Ca}^{2+}/\text{SO}_4^{2-}$ , and they then crystallize into bassanite nanoparticles as the nanoscale precursor emerges. Afterward, bassanite nanoparticles grow into nanorods, and the bassanite nanorods

self-assembled along the c axis grow into larger nanorods, which are finally transformed into gypsum.

- IV. Calcium sulfate nanoparticles could interact with materials and factors in the natural estuarine bay environment, and participate in geological and ecological processes.

**Author Contributions:** Writing—original draft and data analysis, G.W.; conceptualization, supervision, and writing—reviewing and editing, T.Y. and G.W.; sample collection and sample preparation, T.Y.; evidence collection and data curation, Y.F., S.B. and P.Y. All authors have read and agreed to the published version of the manuscript.

**Funding:** This research was funded by the Scientific and Technological Innovation Project of Colleges and Universities in Shanxi Province (2021L273), the Fundamental Research Program of Shanxi Province (202103021223249), the Central Public-interest Scientific Institution Basal Research Fund of China (PM-zx703-202002-043, PM-zx703-202004-152) and the Science and Technology Program of Guangzhou (PM-zx913-202105-165).

**Data Availability Statement:** The data presented in this work are available on request from the corresponding author.

**Acknowledgments:** We thank the Sinoma Institute of Materials Research (Guangzhou) Co., Ltd., for their assistance with the microscopic analysis. We sincerely appreciate the anonymous reviewers for their valuable and constructive comments. Special thanks are extended to Mei Jie for her assistance with English.

**Conflicts of Interest:** The authors declare no conflict of interest.

## References

- Gomis-Yagües, V.; Boluda-Botella, N.; Ruiz-Beviá, F. Gypsum precipitation/dissolution as an explanation of the decrease of sulphate concentration during seawater intrusion. *J. Hydrol.* **2000**, *228*, 48–55. [[CrossRef](#)]
- He, K.; Nie, A.; Yuan, Y.; Ghodsi, S.M.; Song, B.; Firlar, E.; Lu, J.; Lu, Y.P.; Shokuhfar, T.; Megaridis, C.M. In Situ Transmission Electron Microscopy Explores a New Nanoscale Pathway for Direct Gypsum Formation in Aqueous Solution. *ACS Appl. Nano Mater.* **2018**, *1*, 5430–5440. [[CrossRef](#)]
- Wang, Y.; Kim, Y.; Christenson, H.K.; Meldrum, F.C. A new precipitation pathway for calcium sulfate dihydrate (gypsum) via amorphous and hemihydrate intermediates. *Chem. Commun.* **2012**, *48*, 504–506. [[CrossRef](#)]
- Saha, A.; Lee, J.; Pancera, S.M.; Bräeu, M.F.; Kempter, A.; Tripathi, A.; Bose, A. New insights into the transformation of calcium sulfate hemihydrate to gypsum using time-resolved cryogenic transmission electron microscopy. *Langmuir* **2012**, *28*, 11182–11187. [[CrossRef](#)]
- Fu, H.; Jia, C.; Chen, Q.; Jiang, G. Calcium sulfate polymorph evolution dominated by competitive nucleation in gypsum metastable zone. *J. Cryst. Growth* **2017**, *470*, 143–148. [[CrossRef](#)]
- Jia, C.Y.; Wu, L.C.; Fulton, J.L.; Liang, X.R.; De Yoreo, J.J.; Guan, B.H. Structural characteristics of amorphous calcium sulfate: Evidence to the role of water molecules. *J. Phys. Chem. C* **2021**, *125*, 3415–3420. [[CrossRef](#)]
- Ahmed, S.B.; Tlili, M.; Amor, M.B.; Bacha, H.B.; Elleuch, B. Calcium sulphate scale prevention in a desalination unit using the SMCEC technique. *Desalination* **2004**, *167*, 311–318. [[CrossRef](#)]
- Mi, B.; Elimelech, M. Gypsum scaling and cleaning in forward osmosis: Measurements and mechanisms. *Environ. Sci. Technol.* **2010**, *44*, 2022–2028. [[CrossRef](#)]
- Lu, H.; Kan, A.T.; Zhang, P.; Yu, J.; Fan, C.; Work, S.; Tomson, M.B. Phase stability and inhibition of calcium sulfate in the system NaCl/monoethylene glycol/H<sub>2</sub>O. *SPE J.* **2011**, *17*, 187–197. [[CrossRef](#)]
- Singh, N.B.; Middendorf, B. Calcium sulphate hemihydrate hydration leading to gypsum crystallization. *Prog. Cryst. Growth Charact. Mater.* **2007**, *53*, 57–77. [[CrossRef](#)]
- Van Driessche, A.E.S.; Benning, L.G.; Rodriguez-Blanco, J.D.; Ossorio, M.; Bots, P.; García-Ruiz, J.M. The role and implications of bassanite as a stable precursor phase to gypsum precipitation. *Science* **2012**, *336*, 69–72. [[CrossRef](#)]
- Gendrin, A.; Mangold, N.; Bibring, J.P.; Langevin, Y.; Gondet, B.; Poulet, F.; Bonello, G.; Quantin, C.; Mustard, J.; Arvidson, R.; et al. Sulfates in Martian layered terrains: The Omega/Mars express view. *Science* **2005**, *307*, 1587–1591. [[CrossRef](#)]
- Wray, J.J.; Squyres, S.W.; Roach, L.H.; Bishop, J.L.; Mustard, J.F.; Noe Dobra, E.Z. Identification of the Ca-sulfate bassanite in Mawrth Vallis, Mars. *Icarus* **2010**, *209*, 416–421. [[CrossRef](#)]
- Rapin, W.; Meslin, P.Y.; Maurice, S.; Vaniman, D.; Nachon, M.; Mangold, N.; Schröder, S.; Gasnault, O.; Forni, O.; Wiens, R.C.; et al. Hydration state of calcium sulfates in Gale Crater, Mars: Identification of bassanite veins. *Earth Planet. Sci. Lett.* **2016**, *452*, 197–205. [[CrossRef](#)]
- Guan, B.; Yang, L.; Wu, Z.; Shen, Z.; Ma, X.; Ye, Q. Preparation of  $\alpha$ -calcium sulfate hemihydrate from FGD gypsum in K, Mg-containing concentrated CaCl<sub>2</sub> solution under mild conditions. *Fuel* **2009**, *88*, 1286–1293. [[CrossRef](#)]

16. Fu, H.; Guan, B.; Jiang, G.; Yates, M.Z.; Wu, Z. Effect of supersaturation on competitive nucleation of CaSO<sub>4</sub> phases in a concentrated CaCl<sub>2</sub> solution. *Cryst. Growth Des.* **2012**, *12*, 1388–1394. [[CrossRef](#)]
17. Jiang, G.; Fu, H.; Savino, K.; Qian, J.; Wu, Z.; Guan, B. Nonlattice cation-SO<sub>4</sub><sup>2-</sup> ionpairs in calcium sulfate hemihydrate nucleation. *Cryst. Growth Des.* **2013**, *13*, 5128–5134. [[CrossRef](#)]
18. Van Driessche, A.E.S.; Stawski, T.M.; Kellermeier, M. Calcium sulfate precipitation pathways in natural and engineering environments. *Chem. Geol.* **2019**, *530*, 119274. [[CrossRef](#)]
19. Tritschler, U.; Van Driessche, A.E.S.; Kempter, A.; Kellermeier, M.; Cölfen, H. Controlling the selective formation of calcium sulfate polymorphs at room temperature. *Angew. Chem. Int. Ed.* **2015**, *54*, 4083–4086. [[CrossRef](#)]
20. Stawski, T.M.; Van Driessche, A.E.S.; Ossorio, M.; Diego Rodriguez-Blanco, J.; Besselink, R.; Benning, L.G. Formation of calcium sulfate through the aggregation of sub-3 nanometre primary species. *Nat. Commun.* **2016**, *7*, 11177. [[CrossRef](#)]
21. Liu, R.; Lin, X.B.; Wang, G.Q.; Liu, X. Natural N-bearing nanoparticles in sediments of a shallow bay of the south China: A new N form in N-cycling. *Ecol. Indic.* **2021**, *122*, 107281. [[CrossRef](#)]
22. Yon, J.N.; Lead, J.R. Manufactured nanoparticles: An overview of their chemistry, interactions and potential environmental implications. *Sci. Total. Environ.* **2008**, *400*, 396–414.
23. Lu, M.Q.; Cao, J.J.; Wang, Z.Y.; Wang, G.Q. Characteristics of Naturally Formed Nanoparticles in Various Media and Their Prospecting Significance in Chaihulanzi Deposit. *Minerals* **2022**, *12*, 1289. [[CrossRef](#)]
24. Yücel, M.; Gartman, A.; Chan, C.S.; Luther III, G.W. Hydrothermal vents as a kinetically stable source of iron-sulphide-bearing nanoparticles to the ocean. *Nat. Geosci.* **2011**, *4*, 367–371. [[CrossRef](#)]
25. Borm, P.J.; Kreyling, W. Toxicological hazards of inhaled nanoparticles-potential implications for drug delivery. *J. Nanosci. Nanotechnol.* **2004**, *4*, 521–531. [[CrossRef](#)]
26. Craft, E.; Abu-Qare, A.; Flaherty, M.; Garofolo, M.; Rincavage, H.; Abou-Donia, M. Depleted and natural uranium: Chemistry and toxicological effects. *J. Toxicol. Environ. Health Part B* **2004**, *7*, 297–317. [[CrossRef](#)] [[PubMed](#)]
27. Oberdorster, G.; Sharp, Z.; Atudorei, V.; Elder, A.; Gelein, R.; Kreyling, W.; Cox, C. Translocation of inhaled ultrafine particles to the brain. *Inhal. Toxicol.* **2004**, *16*, 437–445. [[CrossRef](#)] [[PubMed](#)]
28. He, J.; Garzanti, E.; Cao, L.C.; Wang, H. The zircon story of the Pearl River (China) from Cretaceous to present. *Earth-Sci. Rev.* **2020**, *201*, 103078. [[CrossRef](#)]
29. Yuan, X.Q.; Yang, Q.S.; Luo, X.X.; Yu, F.L.; Liu, F.; Li, J.Y.; Wang, Z.H. Distribution of grain size and organic elemental composition of the surficial sediments in Lingding Bay in the Pearl River Delta, China: A record of recent human activity. *Ocean. Coast. Manag.* **2019**, *178*, 104849. [[CrossRef](#)]
30. Zhang, Q.; Xiao, M.; Singh, V.P.; Li, J. Regionalization and spatial changing properties of droughts across the Pearl River basin, China. *J. Hydrol.* **2012**, *472–473*, 355–366. [[CrossRef](#)]
31. He, J.; Garzanti, E.; Dinis, P.; Yang, S.; Wang, H. Provenance versus weathering control on sediment composition in tropical monsoonal climate (South China)-1. Geochemistry and clay mineralogy. *Chem. Geol.* **2020**, *558*, 119860. [[CrossRef](#)]
32. Yuan, X.Q.; Yang, Q.S.; Meadows, M.E.; Luo, X.X.; Wang, Z.H. Grain size and organic geochemistry of recent sediments in Lingding Bay, Pearl River Delta, China: Implications for sediment dispersal and depositional processes perturbed by human activities. *Anthr. Coasts* **2021**, *4*, 147–167. [[CrossRef](#)]
33. Chen, S.Z.; Pei, C.M. Geology and geochemistry of source rocks of the eastern Pearl River mouth basin, South China Sea. *J. Asian Earth Sci.* **1993**, *8*, 393–406.
34. Hu, D.; Clift, P.D.; Böning, P.; Hannigan, R.; Hillier, S.; Blusztajn, J.; Wan, S.M.; Fuller, D.Q. Holocene evolution in weathering and erosion patterns in the Pearl River delta. *Geochem. Geophys. Geosyst.* **2013**, *14*, 2349–2368. [[CrossRef](#)]
35. Tang, T. Surface sediment characteristics and tower karst dissolution, Guilin, southern China. *Geomorphology* **2002**, *49*, 231–254. [[CrossRef](#)]
36. Han, G.; Liu, C. Water geochemistry controlled by carbonate dissolution: A study of the river waters draining karst-dominated terrain, Guizhou Province, China. *Chem. Geol.* **2004**, *204*, 1–21. [[CrossRef](#)]
37. Jones, F. Infrared investigation of barite and gypsum crystallization: Evidence for an amorphous to crystalline transition. *CrystEngComm* **2012**, *14*, 8374–8381. [[CrossRef](#)]
38. Wallace, A.F.; Hedges, L.O.; Fernandez-Martinez, A.; Raiteri, P.; Gale, J.D.; Waychunas, G.A.; Whitlam, S.; Banfield, J.F.; De Yoreo, J.J. Microscopic evidence for liquid-liquid separation in supersaturated CaCO<sub>3</sub> solutions. *Science* **2013**, *341*, 885–889. [[CrossRef](#)]
39. Gebauer, D.; Kellermeier, M.; Gale, J.D.; Bergstrom, L.; Colfen, H. Pre-nucleation clusters as solute precursors in crystallisation. *Chem. Soc. Rev.* **2014**, *43*, 2348–2371. [[CrossRef](#)]
40. De Yoreo, J.J.; Gilbert, P.U.P.A.; Sommerdijk, N.A.J.M.; Penn, R.L.; Whitlam, S.; Joester, D.; Zhang, H.; Rimer, J.D.; Navrotsky, A.; Banfield, J.F.; et al. Crystallization by particle attachment in synthetic, biogenic, and geologic environments. *Science* **2015**, *349*, a6760. [[CrossRef](#)]
41. Sun, S.; Chevrier, D.M.; Zhang, P.; Gebauer, D.; Cölfen, H. Distinct short-range order is inherent to small amorphous calcium carbonate clusters (<2 nm). *Angew. Chem. Int. Ed.* **2016**, *55*, 12206–12209.
42. Baalousha, M. Aggregation and disaggregation of iron oxide nanoparticles: Influence of particle concentration, pH and natural organic matter. *Sci. Total Environ.* **2009**, *407*, 2093–2101. [[CrossRef](#)] [[PubMed](#)]
43. Hotze, E.M.; Phenrat, T.; Lowry, G.V.; Loery, G.V.; Bernhardt, E.S.; Dionysiou, D.D.; Wiesner, M.R. Nanoparticle aggregation: Challenges to understanding transport and reactivity in the environment. *J. Environ. Qual.* **2010**, *39*, 1909. [[CrossRef](#)] [[PubMed](#)]

44. Afshinnia, K.; Baalousha, M. Effect of phosphate buffer on aggregation kinetics of citrate-coated silver nanoparticles induced by monovalent and divalent electrolytes. *Sci. Total Environ.* **2017**, *581–582*, 268–276. [[CrossRef](#)]
45. Yang, X.Z.; Wang, Q.; Qu, X.L.; Jiang, W. Bound and unbound humic acids perform different roles in the aggregation and deposition of multi-walled carbon nanotubes. *Sci. Total Environ.* **2017**, *586*, 738–745. [[CrossRef](#)]
46. Cao, J.J.; Hu, X.Y.; Jiang, Z.T.; Li, H.W.; Zou, X.Z. Simulation of adsorption of gold nanoparticles carried by gas ascending from the earth's interior in alluvial cover of the middle–lower reaches of the yangtze river. *Geofluids* **2010**, *10*, 438–446. [[CrossRef](#)]

**Disclaimer/Publisher's Note:** The statements, opinions and data contained in all publications are solely those of the individual author(s) and contributor(s) and not of MDPI and/or the editor(s). MDPI and/or the editor(s) disclaim responsibility for any injury to people or property resulting from any ideas, methods, instructions or products referred to in the content.